Earth and Planetary Science Letters 345–348 (2012) 159–170

Contents lists available at SciVerse ScienceDirect

Earth and Planetary Science Letters

journal homepage: www.elsevier.com/locate/epsl

Letters

Melting phase relations in the MgO–$MgSiO_3$ system between 16 and 26 GPa: Implications for melting in Earth's deep interior

Christian Liebske [a,*], Daniel J. Frost [b,1]

[a] Institute for Geochemistry and Petrology, Clausiusstrasse 25, NW, ETH Zürich, CH-8092 Zürich, Switzerland
[b] Bayerisches Geoinstitut, Universität Bayreuth, Universitätsstrasse 30, D-95447 Bayreuth, Germany

ARTICLE INFO

Article history:
Received 28 January 2012
Received in revised form
13 June 2012
Accepted 19 June 2012
Editor: L. Stixrude

Keywords:
lower mantle
melting
core–mantle-boundary
eutectic composition

ABSTRACT

Melting experiments in the system MgO–$MgSiO_3$ were performed to study the eutectic melt composition and phase relations between 16 and 26 GPa using the mutlianvil apparatus. By employing a multi-chamber capsule design, several different starting compositions along this binary join could be run at a single pressure and temperature and internally consistent phase relations and liquidus compositions were obtained. A single eutectic composition was identified on this join which becomes progressively more MgO-rich over the investigated pressure range. A simple thermodynamic model is developed to describe the melting phase relations based on literature models for melting curves of end-members and a symmetric liquid mixing model.

It is shown that melting relations of a natural peridotite composition at high pressure can be reasonably approximated on the basis of the phase relations of this simple binary, and a very good agreement is found once the effects of FeO on phase relations and melting temperatures are considered.

The thermodynamic model, extrapolated to pressures covering the entire mantle, predicts that the eutectic composition becomes richer in MgO up to approximately 80 GPa, where it becomes near constant with pressure and has a Mg/Si ratio close to that of a peridotite composition. By applying further experimental results to account for the effect of FeO on the melting temperatures, the model predicts that the solidus and liquidus for a peridotitic composition at lower mantle pressures are never more than ~250 K apart.

These results can be used to examine a partial melt origin for the existence of localised zones with ultra low shear wave velocities (ULVZ) at the core–mantle boundary (CMB). The solidus temperature of peridotitic mantle at the CMB is estimated to be 4400 ± 300 K, which would require temperatures at the CMB to be at the very top end of the estimated range for melting to occur. The proximity of the solidus and liquidus temperature predicted by the model, however, implies that large melt fractions could form over small depth intervals as a result of relatively small increases in either temperature or FeO content. This is consistent with a seismically sharp transition in the upper boundary of ULVZ layers. Given the high temperatures required to melt mantle peridotite at the CMB, a partial melt origin due to raised FeO contents seems more plausible.

© 2012 Elsevier B.V. All rights reserved.

1. Introduction

Melting of nominally dry mantle peridotite occurs as the temperature of adiabatically decompressing mantle crosses the peridotite solidus at depths of the order of 50 km (McKenzie and Bickle, 1988). Volatile induced melting, on the other hand, can occur at significantly greater depths with kimberlitic magma genesis, for example, generally considered to occur at depths >150 km (Mitchell, 1986). Melting of the deeper mantle must, for the main part, be confined to regions of enhanced volatile content; however, there are circumstances that may lead, or may have led, to the nominally volatile free melting of the deep lower mantle. Seismic studies, for example, provide evidence for zones of ultra low velocity at the base of the mantle, which have been attributed to the production of silicate melts within the thermal boundary layer at the core mantle boundary (Garnero and Helmberger, 1998; Lay et al., 2004). Models for Earth's accretion also imply a period of substantial deep mantle melting due to the impact of planetesimals and the release of gravitational energy from separating core-forming metal (Tonks and Melosh, 1993; Stevenson, 1990; Canup and Asphaug, 2001). Fractional crystallisation of such a global magma ocean may have led to chemical differentiation of the mantle, which is supported by the isotopic

* Corresponding author. Tel.: +41 44 632 7803; fax: +41 632 1636.
E-mail address: christian.liebske@erdw.ethz.ch (C. Liebske).
[1] Tel.: +49 921 55 3737; fax: +49 921 55 3769.

0012-821X/$ - see front matter © 2012 Elsevier B.V. All rights reserved.
http://dx.doi.org/10.1016/j.epsl.2012.06.038

evolution of some of the Earth's oldest rocks (Boyet and Carlson, 2005). Subsequent mantle convection may have homogenised such chemically fractionated reservoirs or confined them to only the deepest levels of the mantle.

In order to test the likelihood that the base of the lower mantle contains partial melt or to examine the consequences of the crystallisation of a global magma ocean, some appreciation of melting temperatures and phase relations at pressures covering the entire mantle is required. A number of problems complicate the determination of solidus and liquids phase relations for bulk silicate earth compositions at very high pressures. Multianvil experiments, for example, suffer from large thermal gradients that make the onset of melting difficult to detect and make it almost impossible to measure liquid compositions at temperatures below the liquidus (Zhang and Herzberg, 1994; Trønnes and Frost, 2002). The same issues are even more problematic in laser heated diamond anvil cell experiments that also suffer from intense chemical segregation due to large thermal gradients in the heated region (Sinmyo and Hirose, 2010). Without a fundamental understanding of the effect of pressure on silicate melting it becomes difficult to assess the relevance and accuracy of results gained in multianvil apparatus and diamond anvil cell experiments. This limits the implications of melting experiments to only the most qualitative of inferences concerning melting of the deep mantle.

Here melting experiments were performed in the mutlianvil to study the eutectic melt composition in the system MgO–$MgSiO_3$ between 16 and 26 GPa. Changes in the composition of the eutectic found on this join with pressure will cause changes in the liqudius phase assemblage for a given composition, which likely emulate those in complex bulk silicate Earth compositions. The eutectic composition places hard constraints on the thermodynamics of silicate melting and can be used to parameterize thermodynamic models that can be extrapolated to higher pressures. Experiments were performed using multi-chamber capsules where several compositions along the MgO–$MgSiO_3$ join can be exposed simultaneously at a single pressure and temperature. At a given temperature the liquidus on both MgO-rich and $MgSiO_3$-rich sides of the eutectic can be unambiguously bracketed. A simple thermodynamic model has been developed based on melting curves of the MgO and $MgSiO_3$ end member phases and using symmetric two liquid component mixing relations. This model is then compared with existing experimental data in more complex systems and is found to capture and explain most of the important features of these previous results. The model is used to predict melting phase relations throughout the lower mantle to the core mantle boundary (CMB).

1.1. Previous experimental work

Bowen and Anderson (1914) investigated the system MgO–SiO_2 at ambient pressure and Boyd et al. (1964) performed melting experiments on $MgSiO_3$ up to 5 GPa, noting that melting becomes congruent at pressures below 0.54 GPa or at 0.13 GPa according to Chen and Presnall (1975). The congruent melting behaviour of high pressure $MgSiO_3$ phases has been confirmed to lower mantle pressures by Taylor (1973), Kato and Kumazawa (1985a, 1985b), (3, 7, 20 GPa), Presnall and Gasparik (1990) (10–16.5 GPa) and Ito and Katsura (1992) (21–25 GPa).

Forsterite melts congruently at 1 bar and to moderate pressures (Davis and England, 1964), however, some discrepancy exists as to the onset pressure of incongruent melting, to periclase plus liquid, which has been reported to occur at 8.5 GPa (Kato et al., 1998), 10.1 GPa (Presnall and Walter, 1993) and below 12.7 GPa (Ohtani and Kumazawa, 1981). At pressures higher than 15 GPa forsterite melts incongruently to anhydrous phase B (AnhB, $Mg_{14}Si_5O_{22}$) and liquid, which is followed by the reaction AnhB + liquid = periclase + liquid at higher temperatures (Kato and Kumazawa, 1986; Presnall and Walter, 1993). Although Ohtani et al. (1998) reported data on melting of a $(Mg_{0.9},Fe_{0.1})_2SiO_4$ composition between 18 and 25 GPa, no systematic investigation of the melting curve of pure Mg_2SiO_4 to its stability limit (defined by the breakdown to $MgSiO_3$ perovskite plus periclase) has been performed.

Liu and Presnall (1990) determined the eutectic melting composition between Mg_2SiO_4 and $MgSiO_3$ at 2.3 GPa to be 46.5 mol% SiO_2 and other studies have demonstrated that the SiO_2 content of the eutectic melt composition decreases with increasing pressure (Kato and Kumazawa, 1985a, 1990; Presnall and Gasparik, 1990). Data on the Mg_2SiO_4–$MgSiO_3$ eutectic were presented by (Presnall et al., 1998), who reported compositions of 46.3 and 44.4 mol% SiO_2 at 2 and 16.5 GPa, respectively, in good agreement with the aforementioned studies. At higher pressures of approximately 20–23 GPa, data reported by Kato and Kumazawa (1986) and Gasparik (1990) also indicate a decrease in the eutectic SiO_2 content with increasing pressure, although the latter two studies reported relatively large uncertainties in either pressure or composition. The evolution of the eutectic composition as a function of pressure is, therefore, not well constrained above 16.5 GPa.

2. Experimental and analytical methods

Compositions along the join MgO–$MgSiO_3$ were prepared by mixing MgO periclase, Mg_2SiO_4 forsterite, $MgSiO_3$ and SiO_2 glass that had all been previously dried at 1000 °C. Mg_2SiO_4 and $MgSiO_3$ as starting materials were prepared by grinding and mixing the appropriate amounts of analytical grade MgO and SiO_2 under ethanol. The Mg_2SiO_4 mixture was then pressed into a pellet, fired at 1600 °C for 20 h and then ground to a fine powder. This procedure was repeated until powder x-ray diffraction revealed no additional phases. $MgSiO_3$ glass was prepared by melting for 2 h at 1600 °C in a Pt crucible, followed by quenching by dropping the crucible into water. The glass was then ground to a fine powder. Intermediate compositions between periclase (Pc), forsterite (Fo), enstatite (En) and quartz (Qz) were prepared by appropriate mixing of two of these four components. In the following description chemical compositions of starting mixtures used for melting experiments are indicated by mol%, such that a mixture labelled e.g. $Fo_{25}En_{75}$ consists of 25 mol% $MgSiO_4$ and

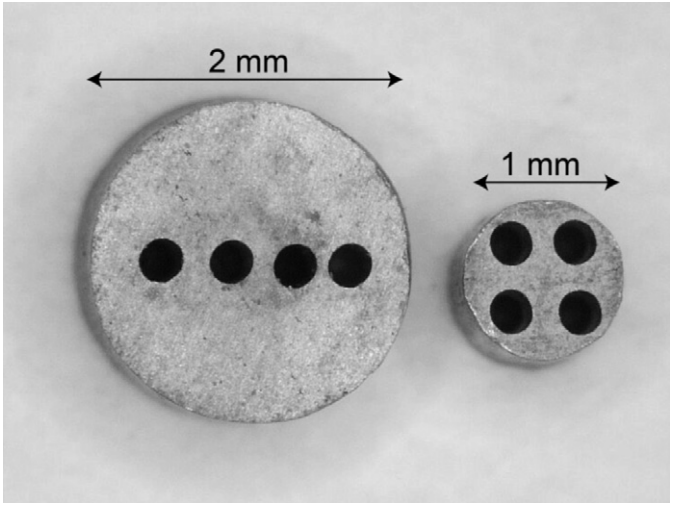

Fig. 1. Multi-chamber capsules with sample chambers drilled by spark erosion from solid Re rods. Each sample chamber hole is approximately 200 μm in diameter and not more than 600 μm deep.

75 mol% $MgSiO_3$. In two experiments at 24 GPa, synthetic fayalite (Fe_2SiO_4) was used to add FeO to the system.

High-pressure melting experiments were performed using multianvil devices at the Bayerisches Geoinstitut. Experiments at 16 and 20 GPa were conducted in a 5000 t press with 18/11 and 18/8 (octahedral edge length/tungsten-carbide anvil truncation in mm) assemblies in combination with 54 mm edge length tungsten carbide anvils. The comparably large 18 mm assemblies allow stepped $LaCrO_3$ heaters to be used, which significantly reduces thermal gradients over the sample length. Further details are given in Frost et al. (2004b) and Keppler and Frost (2005). Experiments at 23–24 GPa and at 26 GPa were carried out in 10/4 and 8/3 mm assemblies, respectively, both in combination with 32 mm tungsten carbide cubes.

At least four starting mixtures were run simultaneously in each experiment by using multi-chamber sample containers with sample holes drilled by spark-erosion from solid rhenium metal rods (Fig. 1). The capsules for the 18 mm assemblies were 2 mm in diameter and approximately 1 mm long, which allowed four sample chamber holes of 250 μm diameter and 600 μm length to be drilled in each capsule. Due to the larger sample volume in the 18 mm pressure cells up to two such multi-chamber capsules could be run in each experiment, separated by Re-foil discs. Capsules in the 10/4 and 8/3 assemblies were 1 mm in diameter and length and were spark eroded with 4 sample chambers. After spark-erosion capsules were cleaned in acetone, left to dry, then fired at 900 °C for 1 min to oxidise carbon residues from the erosion process. The capsules were then further cleaned in ethanol. Different sample powders were loaded into each spark eroded chamber. Compaction of each powder within the chamber with a tungsten needle ensured that powders remained within the chamber. Blowing with air then removed extraneous powders that may have fallen into as yet unfilled chambers. A Re foil disc covered the loading face of the capsule. To ensure anhydrous conditions, ceramic pressure cell parts were fired for several hours at 1000 °C and samples powders were continuously stored in a vacuum furnace at 200 °C. Assembled pressure cells, if not pressurised immediately, were also stored in the vacuum furnace until being used.

Temperature was measured using a $W_{97\%}Re_{3\%}$–$W_{75\%}Re_{25\%}$ thermocouple inserted axially into the assembly with the hot junction in contact with the base of the Re-capsule. Capsules were positioned into the assembly with the loading face directed away from the thermocouple. No correction for the effect of pressure on the thermocouple emf was applied. Run temperatures recorded by the thermocouples varied within ± 10 °C of the reported values during the experiments. In some instances thermocouples failed during compression or heating and temperatures were estimated based on the electrical power applied to the furnace. In some early experiments copper wire coils were used to ensure connectivity of the thermocouple wires as they crossed the pyrophyllite gaskets. In later experiments these coils were fabricated from the corresponding thermocouple wire. A difference in temperature–power relations was observed between the two types of coils that corresponded to temperatures being approximately 200 K higher when copper was not employed (Nishihara et al., 2006). Based on phase relations and power curves for both coil types all temperatures were corrected to those obtained using coils made from thermocouple wire.

Recovered samples were prepared as polished sections, such that all sample chambers were exposed parallel to the cylindrical axis of the capsules in order to observe the phase relations along the thermal gradient, which is parallel to the furnace axis. Mineral phases were identified by micro-Raman spectroscopy. Reference spectra were taken from McMillan et al. (1996) and references therein. Chemical compositions of run products were determined using a Jeol JXA-8200 microprobe at ETH Zürich. Analyses were performed at an acceleration voltage of 15 kV and at various beam currents and diameters. Mineral phases were analysed with beam currents of 10–15 nA and a focused electron beam. Silicate melts, which consist entirely of an intergrowth of quench-crystals, were measured with beam currents of 15–30 nA and beam diameters ranging from 10 to 50 μm. Counting times were 20 s on

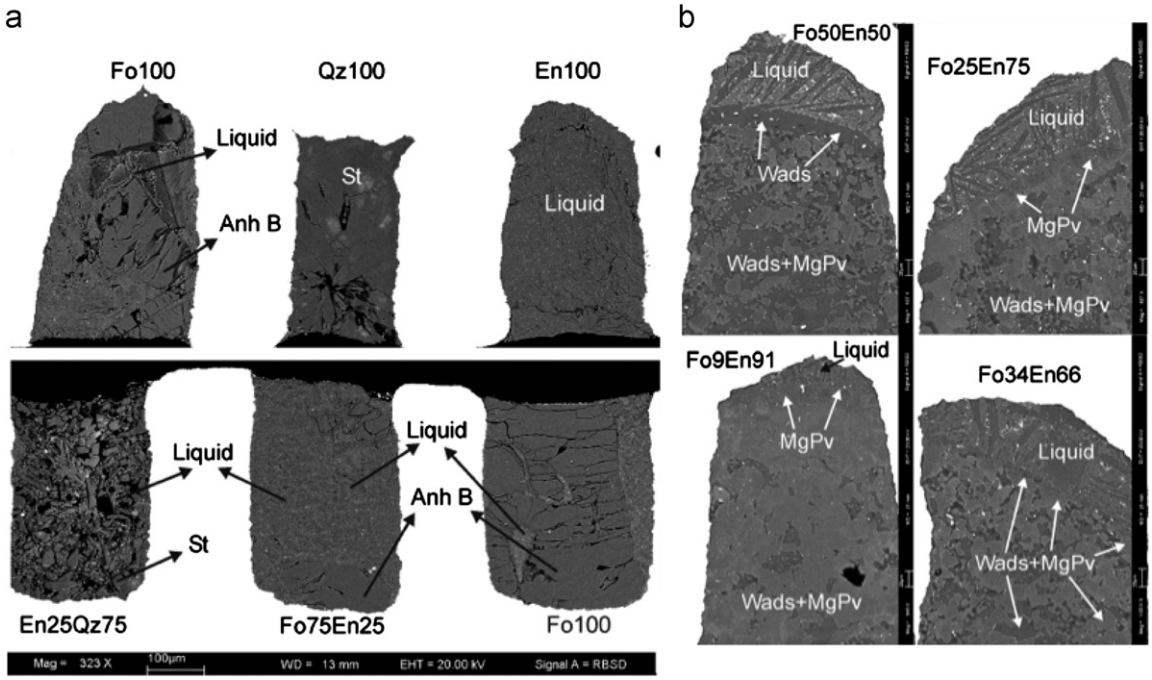

Fig. 2. Back scattered electron images of recovered experimental multi-chamber capsule samples from (a) 16 GPa; run Z282 and (b) S3473 at 23 GPa. Abbreviations are for staring compositions as reported in Tables S1–S5 in the supplementary information. Note that the separation of liquid and solid is less pronounced in the 16 GPa sample, which is attributed to the use of 18 mm pressure cells, stepped heaters and therefore reduced thermal gradients.

the peak and 10 s on the background for each element. Synthetic enstatite and forsterite were used as standard for Si and Mg.

3. Results

Examples of typical multi-chamber capsule experiments are shown in Fig. 2. The three possible types of assemblage, subsolidus, liquidus and super-liquidus are easy to differentiate texturally. Quenched melt forms anhedral aggregates of fine crystals with a generally distinct fabric, while coexisting crystals or subsolidus assemblages form euhedral well crystallised assemblages with clearly developed triple junctions. The resulting experimental assemblages and melt analyses are reported in the Supplementary material in Tables S1–S5. Melting phase relations at experimentally investigated pressures are shown in Fig. 3a–e. Melt compositions analysed using the electron microprobe are indicated in the corresponding figures. Subsolidus assemblages are plotted at the corresponding starting bulk compositions. The underlying phase diagrams between MgO and MgSiO3 were calculated using the software package Perple_X (Connolly, 1990), employing the equations of states and the thermodynamic model discussed below.

3.1. Melting relations at 16 GPa

Experiments at 16 GPa were performed between 2533 and 2733 K. The lowest temperature experiment, Z294, was very close to the eutectic as chambers containing both Mg_2SiO_4 wadsleyite and $MgSiO_3$ majorite were found to each coexist with liquids containing 45.5(10) and 44.1(4) mol% SiO_2 respectively. This implies a eutectic composition of approximately 45 mol% SiO_2, which is in good agreement with the value of 44 mol% previously reported based on experiments at the same pressure performed by Presnall and Gasparik (1990). The estimated solidus temperature of 2500 K is also in good agreement with values of 2513–2523 K reported by Presnall and Gasparik (1990) but is higher than the 2400 K estimate of Kato and Kumazawa (1990). Experiment Z282 indicates that Mg_2SiO_4 wadsleyite melts incongruently at temperatures slightly lower than 2593 K to an assemblage of liquid plus an MgO-rich phase with the stoichiometry $Mg_{14}Si_5O_{24}$ identified as anhydrous phase B (Finger et al., 1991). While experiment Z728 indicates that at temperatures slightly below 2637 K anhydrous phase B melts incongruently to produce periclase (Pc)+liquid. At the highest temperature of 2733 K (Z295) the recovered capsule contained only molten samples, but the measured melt composition in each chamber differed from the initial starting compositions. This may result from either contamination of the initial compositions during loading of the capsule or due to some melt exchange during the experiment. Experiments Z282 and Z297 further locate a eutectic composition in the system $MgSiO_3$–SiO_2 at a molar SiO_2 concentrations <51.1 (3)%, thus compositionally very close to the $MgSiO_3$, which likely implies a eutectic temperature only slightly lower than the majorite melting point.

3.2. Melting relations at 20 GPa

Experiments at 20 GPa were performed between 2544 and 2750 K. The eutectic was tightly constrained by the conditions of experiment Z445 performed at 2596 K in which majorite and wadsleyite were found to coexist in several individual chambers with a liquid containing on average 44.0 (5) mol% SiO_2. Wadsleyite appears to melt incongruently to periclase plus liquid, below 2642 K. If a field of anhydrous phase B plus liquid still exists at this pressure, it would have to be between 2596 and 2642 K, which seems unlikely. The peritectic point at the junction of the liquidus curves Pc+Liq and Wads+Liq has a molar SiO_2 concentration of approximately 42%.

3.3. Melting relations at 23 GPa

Experiments at 23 GPa were performed at approximately 2593 and 2693 K. Thermocouples in these experiments failed during heating and electrical power was used to estimate temperatures. The eutectic liquid composition could be determined from experiments S3468 and S3473, both performed at ~2693 K in which all chambers contained melt (see Fig. 2b) of a similar composition, coexisting with either wadsleyite, perovskite or both phases. The weighted average eutectic liquid composition is 43.7 (7) mol% SiO_2. Experiment S3462 at ~2593 K crystallised a subsolidus assemblages of wadsleyite, and perovskite, however in the colder end of each chamber ringwoodite (Rwd) replaced wadsleyite. This indicates that the Mg_2SiO_4 wadsleyite to ringwoodite transition occurs within approximately 200 K of the solidus at 23 GPa, assuming a thermal gradient of the order of ~200 K/mm.

3.4. Melting relations at 24 GPa

Experiments at 24 GPa were performed between 2640 K and 2873 K. Experiment H3126 at 2764 K contains melt at the lowest temperature, which coexists with periclase. Although perovskite was identified in another chamber in this experiment no coexisting liquid could be identified. The eutectic composition can instead be bracketed between experiment H3126, where liquid coexisting with periclase contains 43 (1)% SiO_2, and experiment S3415 at 2800 K where liquid coexisting with perovskite contains 43.3 (12)%. All subsolidus assemblages contained perovskite and periclase. Run S3415 also brackets the location of the eutectic between $MgSiO_3$ and SiO_2 to be <50.9 (7) mol% SiO_2.

The starting compositions containing Fe_2SiO_4 (H3126, H3120) produced an assemblage of ferropericlase (Mg,Fe)O plus liquid (see Table S4 for compositions). In both cases by comparing the SiO_2 content of the liquid with the corresponding Fe-free liquid composition, it is possible to determine the shift of the liquidus curve resulting from the addition of the FeO. As shown by the dashed curve in Fig. 6 the liquidus curve is shifted downward in temperature by approximately 250 K compared to the Fe-free liquidus curve.

3.5. Melting relations at 26 GPa

Experiments were performed between approximately 2800 and 2873 K with temperatures estimated from electrical power consumption. Although all mixtures in sample H2366 share a common eutectic temperature, small melt layers towards the capsule walls coexisting with MgPv were only observed in two out of the four samples. It is not clear whether melt in the remaining two chambers ($Fo_{50}En_{50}$, $Fo_{75}En_{25}$) was either not exposed during polishing or did not form, possibly as a result of a radial thermal gradient and a non-symmetrical distribution of the sample chamber across the container. The same effect is probably responsible for the inconsistent result at 2873 K (H2146), where the compartment containing En_{100} seems entirely melted, while Fo_9En_{91} contains MgPv on the liquidus. In sample H2367 two samples were lost during polishing and the remaining compositions ($Fo_{50}En_{50}$, $Fo_{75}En_{25}$) resulted in a phase assemblage of liquid and periclase. The eutectic composition at 26 GPa can therefore be inferred from both experiments, H2366 and H2367, to be approximately located at 42.4 (10) mol% SiO_2. One sample chamber in run H2154 showed the presence of isolated melt

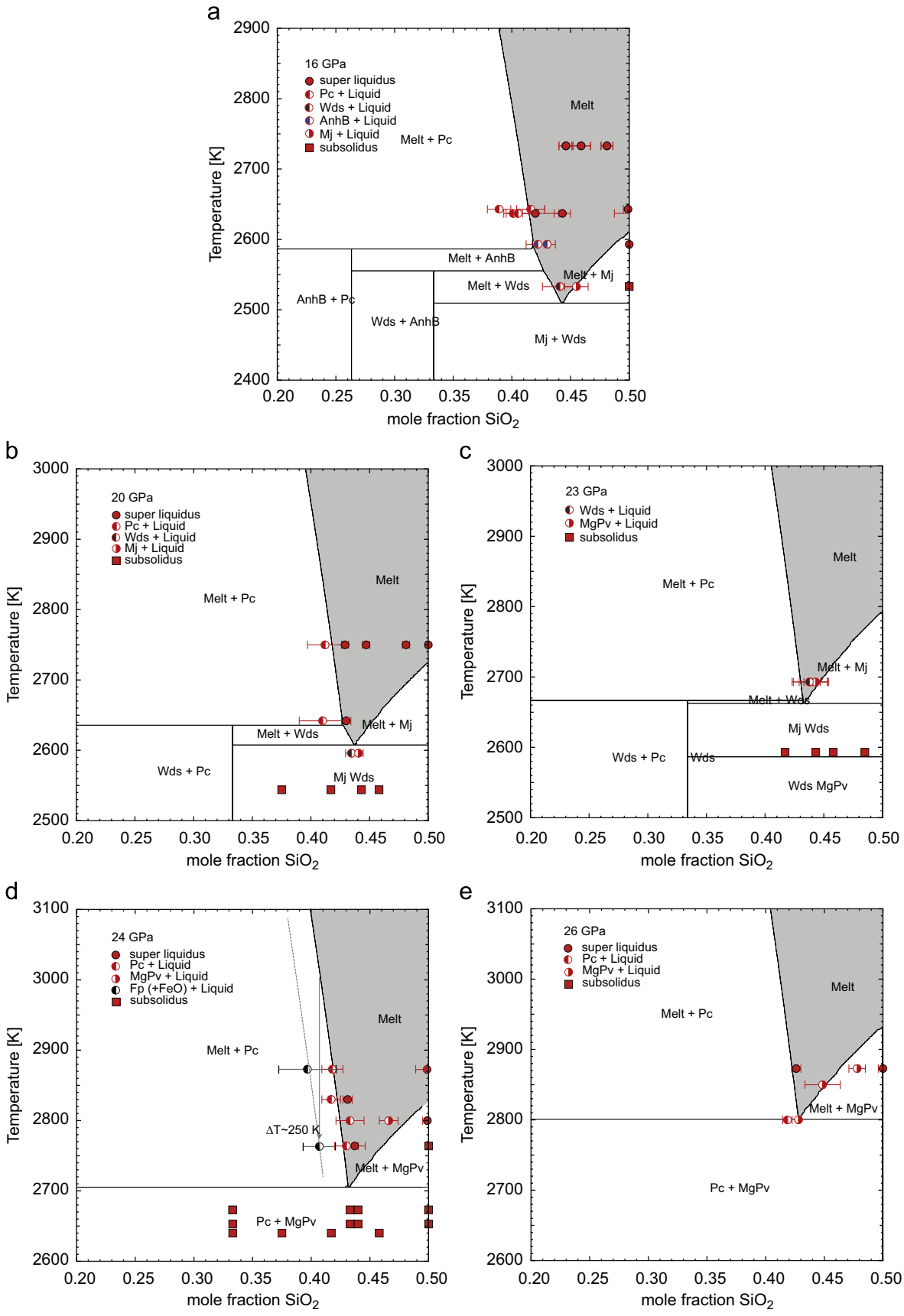

Fig. 3. (a–e) Experimentally observed phase relations and calculated phase diagrams at 16, 20, 23, 24 and 26 GPa. Note that chemical compositions are reported and displayed as mole fractions SiO_2, which can take values from 0 to 0.5 in the pseudo end-member system MgO–$MgSiO_3$. Samples that show a subsolidus phase assemblage are indicated by filled squares compositionally located at their respective starting composition. Liquidus compositions determined from electron microprobe analyses are plotted as half filled circles, with the colour indicating the solid phase with which the liquid is in equilibrium. Totally molten samples are shown as filled circles. Fig. 3c: At 23 GPa the model still predicts majorite to be stable, whereas MgPv is observed experimentally as the stable $MgSiO_3$ polymorph. Performing the calculation at slightly higher pressures (+0.4 GPa) stabilizes perovskite (MgPv) over majorite (Mj), which is within the experimental uncertainties. Fig. 3d also indicates the depression of the liquidus curve due to the addition of FeO to the system. Abbreviations: Liq—silicate liquid, Pc—periclase, AnhB—anhydrous phase B, Wds—wadsleyite.

pools coexisting with $MgSiO_3$ perovskite. The melt composition in the sample chamber initially containing $MgSiO_3$ (En_{100}) is slightly more Si-rich than pure $MgSiO_3$ (51.5 (13) mol% SiO_2). This is probably the result of a small amount of contamination of this sample chamber during capsule loading.

4. Thermodynamic model

It can be shown that a relatively simple thermodynamic model can reproduce the experimental data on the composition and approximate temperature of the eutectic in the MgO–$MgSiO_3$ subsystem. The model depends, for the main part, on previous thermodynamic determinations for the melting curves of MgO and $MgSiO_3$ phases. Note, that the component $MgSiO_3$ should be considered as a pseudo end-member as the entire chemical system extends to pure SiO_2. This means, for example, that the model could never be extended for use at ambient pressure, because at these conditions $MgSiO_3$ melts incongruently to produce forsterite plus a liquid more rich in SiO_2 than $MgSiO_3$ (Bowen and Anderson, 1914). However, this simplified pseudo system suffices for a description of melting in the transition zone and lower mantle.

At the eutectic, the chemical potentials μ_{MgO} and μ_{MgSiO_3} for MgO and $MgSiO_3$ in the solid and liquid phases are equal, such that

$$\mu^{solid}_{MgO} = \mu^{liq}_{MgO}, \quad (1)$$

$$\mu^{solid}_{MgSiO_3} = \mu^{liq}_{MgSiO_3}. \quad (2)$$

As the solid phases remain pure at all conditions these equations can be expanded as

$$\mu^{solid}_{MgO} = \mu^{O,liq}_{MgO} + RT\ln(a_{MgO}) \quad (3)$$

$$\mu^{solid}_{MgSiO_3} = \mu^{O,liq}_{MgSiO_3} + RT\ln(a_{MgSiO_3}) \quad (4)$$

where $\mu^{O,liq}_{MgO}$ and $\mu^{O,liq}_{MgSO_3}$ are the standard state chemical potentials of the pure end member liquids and a_{MgO} and a_{MgSiO_3} are the activities of the MgO and $MgSiO_3$ components in the liquid. For MgO, for example

$$a_{MgO} = X_{MgO}\gamma_{MgO} \quad (5)$$

where X_{MgO} is the mole fraction of MgO in the MgO–$MgSiO_3$ liquid and γ_{MgO} is the activity coefficient of the MgO component in the liquid. The activity of the $MgSiO_3$ component is determined similarly, recognising that $X_{MgSiO_3} = 1 - X_{MgO}$. Activity composition relations are then described using a binary symmetric solution expression:

$$RT\ln\gamma_{MgO} = W_{MgO-MgSiO_3}(1-X_{MgO})^2 \quad (6)$$

$$RT\ln\gamma_{MgSiO_3} = W_{MgO-MgSiO_3}(1-X_{MgSiO_3})^2 \quad (7)$$

where $W_{MgO-MgSiO_3}$ is a Margules interaction parameter. Standard state chemical potentials, e.g. $\mu^{O,liq}_{MgO}$ and $\mu^{O,solid}_{MgO}$, can be evaluated from thermodynamic models in the literature derived to describe the melting curves of MgO and $MgSiO_3$ phases. The melting curve of MgO, for example, is determined through the condition of equilibrium:

$$\mu^{O,liq}_{MgO} - \mu^{solid}_{MgO} = 0 = \overline{G}_{f,MgO} \quad (8)$$

where $\overline{G}_{f,MgO}$ is the Gibbs free energy of fusion. Similar expressions can be derived for $MgSiO_3$ phases. In this study the standard state chemical potentials for the solid end members are calculated using the equation of state (EOS) of Stixrude and Lithgow-Bertelloni (2011). The liquid phases are described using the model and parameters from de Koker and Stixrude (2009). The equations to calculate end-member properties are summarised in the Supplementary material.

Melting curves for MgO and $MgSiO_3$ calculated from these models are shown in Fig. 4. Our own data provide the best constraint on the melting of $MgSiO_3$ perovskite at 24 ± 1 GPa, where it is found to occur below 2837 ± 30 K and above 2764 ± 30 K, which is in excellent agreement with data from Ito and Katsura (1992) at 25 GPa, determined in the multianvil.

Uncertainties on melting curves were calculated using a Monte Carlo simulation technique by randomly varying the EOS parameters for both liquid and solid end-members within their absolute range of uncertainties as reported by de Koker and Stixrude (2009) and Stixrude and Lithgow-Bertelloni (2011). The lower and upper limits of the melting curves represent the minimum and maximum observed melting temperatures from 500 simulations at each pressure. The model $MgSiO_3$ perovskite melting curve predicts temperatures slightly lower than diamond anvil cell measurements (Zerr and Boehler, 1993; Shen and Lazor, 1995) but higher than a recent curve based on the shock experiments (Mosenfelder et al., 2009). However, the melting curve of Mosenfelder et al. (2009) is within the model uncertainties and most diamond anvil cell measurements are within 200 K of these uncertainties.

Similarly, the simulated uncertainty of the MgO melting curve is in agreement with most of the previous melting curve determinations (e.g. Alfe, 2005; Belonoshko and Dubrovinsky, 1996). The ab-initio melting curve of Cohen and Gong (1994), the latter being consistent with recent experimental data of Zhang and Fei (2008), has a steeper Clapeyron slope and higher absolute values compared to the fusion curve of de Koker and Stixrude (2009) at low pressure, but both converge within the range of uncertainty at pressures towards the core–mantle boundary. On the other hand the MgO melting curve of Zerr and Boehler (1994) is significantly lower in terms of absolute temperature and Clapeyron slope. However, the liquidus curve for MgO in the MgO–$MgSiO_3$ system determined in this study (shown in Fig. 3d

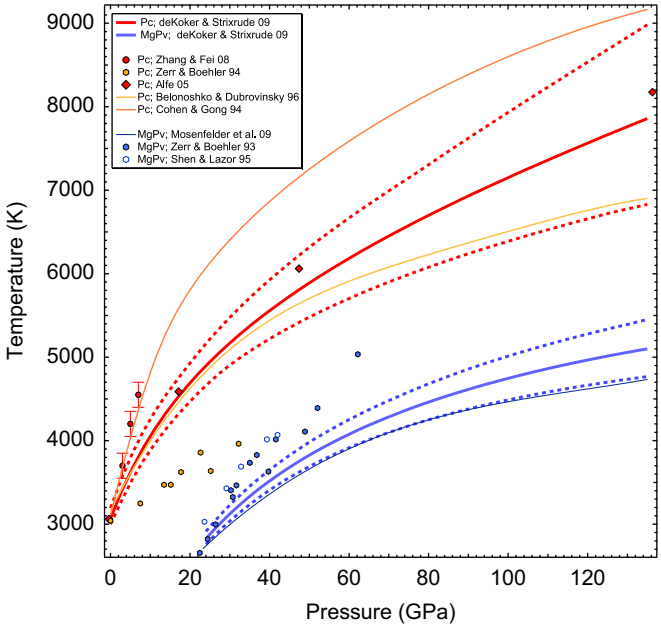

Fig. 4. Melting temperatures of MgO and $MgSiO_3$ perovskite from various experimental and computational studies. The melting curves of de Koker and Stixrude (2009) are used to determine the end member liquid properties for the MgO–$MgSiO_3$ thermodynamic melting model. Red and blue dashed lines (for Pc and MgPv, respectively) represent the minimum and maximum melting temperatures obtained from Monte Carlo simulations (see text for details).

for example) is too steep to be compatible with the Zerr and Boehler (1994) MgO melting curve. Therefore, the melting curves by de Koker and Stixrude (2009), which define the end-member properties of our thermodynamic model, reasonably reproduce the available experimental and computational data.

The eutectic composition can be determined using the thermodynamic model at any pressure by solving Eqs. (3) and (4) simultaneously to determine temperature and X_{MgO} using the aforementioned models for liquid and solid MgO and $MgSiO_3$ to calculate the standard state chemical potentials. The Margules parameter $W_{MgO-MgSiO_3}$ can then be refined to provide an optimal fit between the experimental and thermodynamically determined phase relations. Through this procedure it was found that the experimental results could be reproduced satisfactorily by using a single value for $W_{MgO-MgSiO_3}$ over the experimental pressure range of 16–26 GPa. However, such a model would fail to reproduce eutectic compositions at lower pressures (<16 GPa) where the interaction parameter must assume a higher value. To resolve this, an empirical expression was derived:

$$W_{MgO-MgSiO_3} = A + \frac{B}{P} \quad (9)$$

where P is pressure in GPa and A and B are constants which assume values of -43 kJ/mol and 1.1×10^5 kJ*GPa/mol when refined to the experimental data. Using this expression, $W_{MgO-MgSiO_3}$ becomes near constant above 30 GPa up to 140 GPa at approximately -42 kJ/mol. Such a near constant interaction parameter at higher pressures is consistent with results from de Koker (2008) showing a negligible change in excess volume between mixing of MgO and SiO_2 above 25 GPa. Note that Eq. (9) implies a positive excess volume at low pressure decreasing towards ideal mixing at high pressure. Fig. 3a–e shows phase diagrams and liquidus curves calculated with this thermodynamic model. The calculated liquidus curves are in most instances in excellent agreement with experimentally determined liquid compositions and phase relations. It should be noted that the model is too simplistic to describe melting phase relations below 10 GPa as it cannot reproduce the congruent melting of forsterite for which a more complicated liquid activity model is required.

5. Discussion

From the experimental and thermodynamically modelled phase relations it is possible to assess solidus and liquidus temperatures for a given bulk composition more reliably than would be achieved by performing a series of experiments at various temperatures with a single bulk composition. However, the results also compare relatively well with experiments performed at high pressure on natural and synthetic peridotite compositions, particularly once the effects of FeO on the melting relations are considered.

Melting experiments on a peridotite bulk compositions performed at 24 GPa reveal a solidus temperature of approximately 2423 K and a liquidus of 2623 K, with ferropericlase being the final phase to melt at the liquidus (Trønnes and Frost, 2002). In the simple MgO–$MgSiO_3$ system a peridotite composition, represented by a molar SiO_2 concentration of 42% (i.e. $SiO_2/[SiO_2+MgO]\times100$), would have solidus and liquidus temperatures of 2700 and 2850 K, respectively, as can be seen from Fig. 3d. To make the comparison more realistic, however, the effect of FeO on melting point depression can be estimated using the results of FeO-bearing experiments performed at 24 GPa and assuming that melting temperatures are depressed proportionally to the mole fraction of FeO in the liquid, for small ranges of melt FeO content. From these experiments the depression in melting temperature caused by 6.5 mol% FeO in the liquid is 280 K (see Fig. 3d). As a simplified peridotitic bulk composition with a Mg-number Mg/(Fe+Mg) of 0.9 will contain 5.8 mol% FeO, this will cause a depression of the liquidus by 250 K, from 2850 to 2600 K, which would bring the simplified MgO–$MgSiO_3$ peridotite liquidus estimate into excellent agreement with the results of Trønnes and Frost (2002) on a natural peridotite composition (2623 K). At the solidus, the concentration of FeO in the liquid can be calculated to be 9.9% FeO by examining the Fe–Mg exchange distribution coefficients K_d^{Fp-liq}, e.g.

$$K_d{}^{Fp-liq} = [x(Fe)^{Fp}/x(Mg)^{Fp}]/\,[x(Fe)^{liq}/x(Mg)^{liq}], \quad (10)$$

between Mg-perovskite and ferropericlase (Fp), perovskite and liquid and ferropericlase and liquid (Trønnes and Frost, 2002). This amount of FeO would cause a depression of the solidus by approximately 400 K, from initially 2700 to 2300 K. This temperature is lower than the value of 2423 K reported by Trønnes and Frost (2002) for natural peridotite solidus at 24 GPa but is still a reasonably good estimate given the experimental uncertainties and the simplification of the model system, as discussed later.

Fig. 5 shows the evolution of the eutectic composition in the MgO–$MgSiO_3$ system as a function of pressure. The eutectic becomes progressively less SiO_2-rich in the investigated pressure range. Extrapolation of the thermodynamic model indicates that this reduction in SiO_2 levels off at high pressure and the eutectic composition is predicted to become relatively constant above 50 GPa. Fig. 5 also indicates that the predicted eutectic composition crosses that of a peridotite or bulk silicate earth (BSE) composition at approximately 33 GPa. At this pressure the simplified mantle composition in the binary system would melt congruently, but at higher pressures the liquidus phase will change from periclase (<33 GPa) to Mg-perovskite (>33 GPa) because the bulk composition now lies on the SiO_2-rich side of the eutectic. Such a transition in liquidus phase has indeed been observed in experiments performed on peridotite composition at approximately 31 GPa (Ito et al., 2004), in almost perfect agreement with the current prediction. Mg-perovskite will therefore be the liquidus phase in a BSE composition throughout most of the pressure range of the lower mantle.

Using the same Monte Carlo simulation approach as described above we have also explored the uncertainty in the eutectic

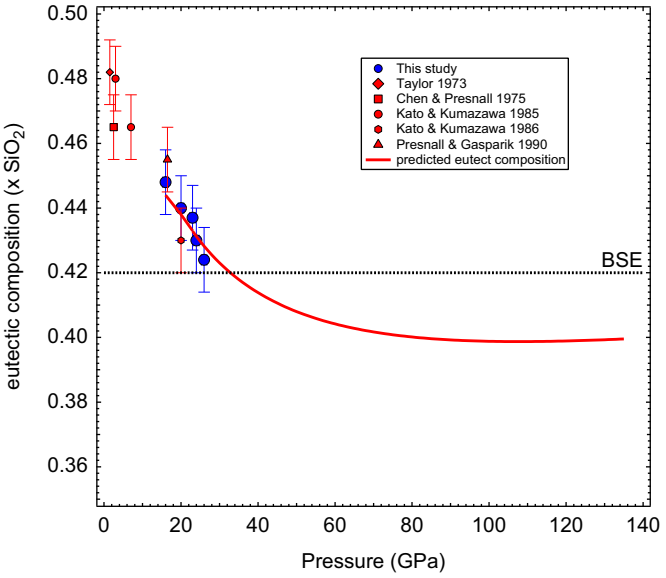

Fig. 5. Experimentally determined eutectic liquid compositions expressed as mole fraction SiO_2 in a SiO_2–MgO liquid. The eutectic composition calculated from the MgO–$MgSiO_3$ melting model is shown by the solid curve. The analogue BSE composition in this system corresponds to an SiO_2 mole fraction of 0.42.

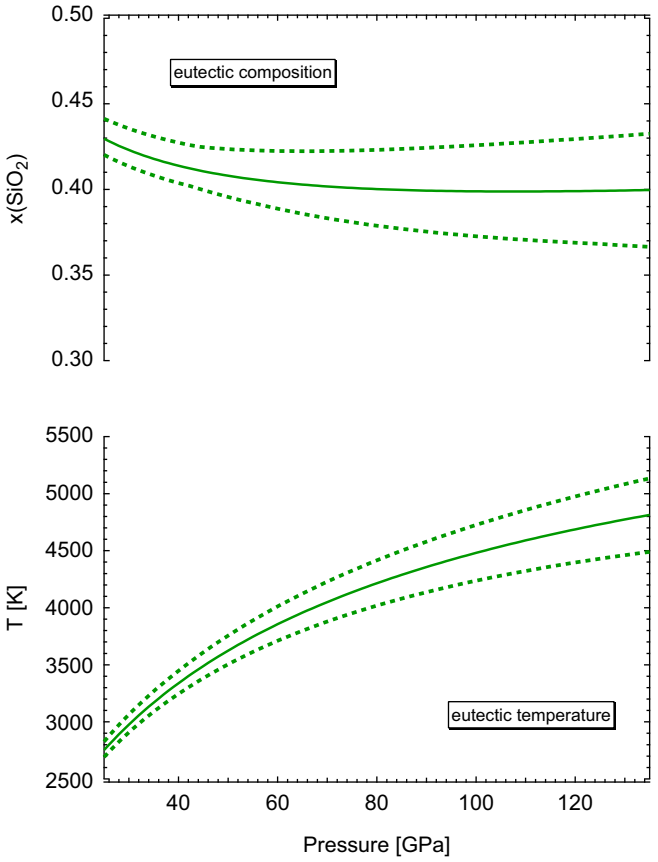

Fig. 6. Model uncertainties for the eutectic composition and the eutectic temperature as a function of pressure based on Monte Carlo simulations. Minimum and maximum compositions and temperatures are minimum and maximum observed values from 500 simulations at each pressure by randomly varying the EOS parameters of the end-members within their uncertainty and by adding a $\pm 10\%$ error of the parameters *A* and *B* describing the interaction parameter *W*.

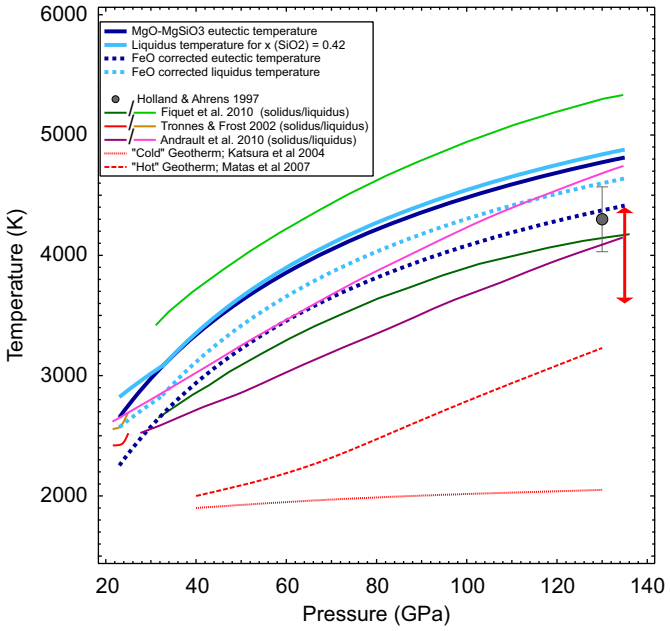

Fig. 7. Summary of solidus and liquidus temperatures in the simple MgO–$MgSiO_3$ system for a simplified BSE bulk composition (SiO_2/[SiO_2+MgO]=0.42).The coarse dotted lines show the solidus and liquidus corrected for the presence of FeO. Results from previous experimental studies on natural bulk compositions are also shown for comparison. The red vertical double arrow at 135 GPa indicate the range of estimates for the outer core temperature at the core mantle boundary. Red dashed lines represent "hot" and "cold" estimates of mantle geotherms (Matas et al., 2007; Katsura et al., 2004). The FeO corrected model predicts BSE melting at the base of the mantle only if temperatures are close to the higher end of those estimated for the outer core temperature.

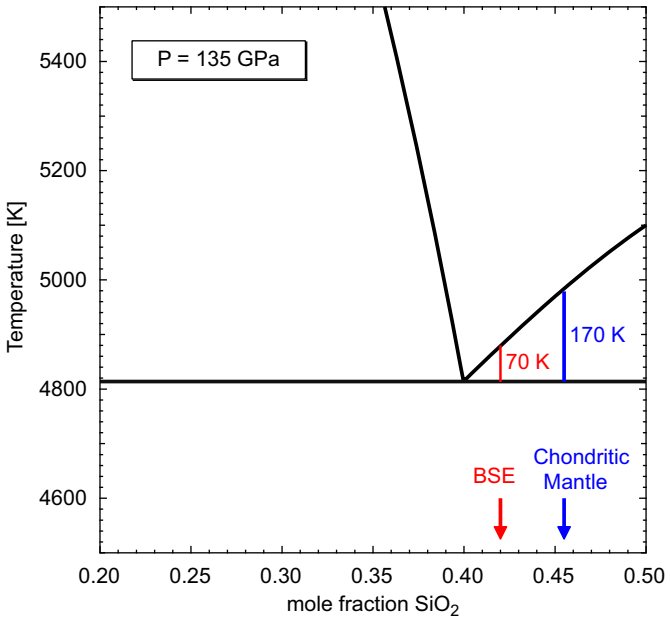

Fig. 8. Predicted phase diagram for the MgO–$MgSiO_3$ sub-system at 135 GPa. Simplified model compositions for the bulk silicate Earth (BSE) and a chondritic mantle composition from Andrault et al. (2011) are shown with the melting temperature interval indicated.

composition and the eutectic temperature considering the uncertainties of the EOS parameters of the end-members and by adding an estimated 10% error to the constants A and B of the expression for the interaction parameter *W* (Eq. (9)). The results are shown in Fig. 6. For the eutectic composition, the error at 30 GPa is around ± 1 mol% SiO_2, which is identical to the experimental uncertainty between 16 and 26 GPa, and for the CMB we predict a eutectic composition $\pm \sim 3$ mol%. The model uncertainty in the eutectic temperature at the CMB is estimated to be ± 300 K.

Fig. 7 summarises liquidus and solidus temperatures for a simplified peridotite composition (i.e. 42% SiO_2) in the system MgO–$MgSiO_3$ as a function of pressure throughout the lower mantle. For the binary the melting interval between solidus and liquidus contracts in temperature up to 33 GPa where the eutectic crosses the 42% SiO_2 bulk composition. The solidus and liquidus separate again at higher pressures but are predicted to be never more than 100 K apart even at the core mantle boundary. This very narrow melting interval is a consequence of the nearly constant eutectic composition above 50 GPa, a bulk composition that is only slightly richer in SiO_2 compared to the eutectic and a relatively shallow liquidus curve between the eutectic and the melting point of $MgSiO_3$.

Melting temperatures in the simple binary will be higher compared to more complex systems that include FeO and other oxides. However, applying a correction for the presence of FeO as discussed previously to estimate the melting behaviour of a chemically more complex peridotite/BSE composition results in the dashed lines in Fig. 7 for the solidus and liquidus. The FeO corrected solidus–liquidus interval is predicted to increase to a value of approximately 230 K at the CMB where the solidus is located at 4400 K (± 300 K; assuming the same error as for the MgO–$MgSiO_3$ system), in excellent agreement with shock wave data for melting of $(Mg,Fe)_2SiO_4$ (Holland and Ahrens, 1997).

However, the small melting temperature interval deviates strongly from that reported in the recent laser heated diamond anvil cell study on a BSE composition by Fiquet et al. (2010), which is of the order of 800 K at 30 GPa and over 1000 K at the CMB. Multianvil experiments on similar natural compositions at 24 GPa predict also a much narrower melting interval than found in these diamond anvil experiments (Trønnes and Frost, 2002; see Fig. 7). Similar diamond cell experiments performed by Andrault et al. (2011) on a slightly more SiO_2-rich "chondritic" composition containing 6.2 mol% FeO are in better agreement with the model developed in this study with respect to the expected melting interval. Andrault et al. (2011) find a solidus temperature of approximately 4150 K at the CMB and a melting interval for this composition of approximately 575 K. As the MgO–$MgSiO_3$ eutectic is closer in composition to the BSE compared to this "chondritic" bulk composition, as indicated in Fig. 8, the estimated melting interval for the latter must be wider than for BSE. The temperature interval from our analysis including FeO for a chondritic composition would be approximately 350 K, which is still in very reasonable agreement with the experimental data of Andrault et al. (2011) considering the uncertainties.

5.1. Effects of other components on melting temperatures

It is important to consider whether the presence of other components in chemically complex mantle compositions could significantly influence the melting phase relations in the lower mantle compared to the simpler model system described above. The oxides MgO, SiO_2 and FeO sum up to approximately 95 mol% of the BSE composition and, as seen, melting phase relations estimated within this simplified system are in good agreement with experiments performed in more complex systems, at least between 24 and 33 GPa (Trønnes and Frost, 2002; Ito et al., 2004). A strong influence of further components, particularly on the lower mantle solidus, might be anticipated if their addition to the system results in the formation of phases with low melting temperatures or, similarly, if they are strongly incompatible during melting.

A BSE composition contains approximately 2 mol% Al_2O_3, which in the lower mantle partitions almost entirely into Mg-perovskite at subsolidus temperatures (Wood, 2000). The partition coefficient describing the Al_2O_3 distribution between Mg-perovskite and silicate melt (D_{Al}=wt%$(Al_2O_3)_{MgPv}$/wt%$(Al_2O_3)_{liq}$) is approximately 0.9 (Trønnes and Frost, 2002; Ito et al., 2004; Liebske et al., 2005) at pressures between 24 and 33 GPa, which implies a potentially small influence on melting temperatures. This is supported by melting experiments at 25 GPa in the $MgSiO_3$–$Mg_3Al_2Si_3O_{12}$ system which even support a small increase in the solidus temperature in Al_2O_3-bearing systems (Kudo and Ito, 1996). A further uncertainty is the combined effect of Al_2O_3 and Fe_2O_3 coupled substitution into Mg-perovskite, which is known to occur even at low oxygen fugacities (Frost et al., 2004a). The presence of this perovskite component is certainly unlikely to strongly lower the mantle solidus as it would have been recognisable in earlier experiments (Trønnes and Frost, 2002; Ito et al., 2004).

At lower mantle conditions CaO is incorporated into calcium-silicate perovskite (CaPv; $CaSiO_3$). At 33 GPa Ito et al. (2004) noted that there is little temperature difference between the disappearance of CaPv and ferropericlase downwards in temperature from the liquidus, in contrast to the observation at 24 GPa (Trønnes and Frost, 2002). This implies that CaPv may be present above the solidus at pressures above 33 GPa and its field of temperatures stability is likely expanding compared to the other phases. This would be consistent with the steep fusion curve of CaPv with pressure (Zerr et al., 1997). For this reason CaO likely has a minor effect on the mantle solidus temperature at lower mantle pressures.

The minor element components, TiO_2, Cr_2O_3, NiO and Na_2O, plus trace elements sum up to a total of 0.6–0.7 mol% in bulk mantle compositions. The effects of minor elements on depressing the solidus temperature can be qualitatively assessed by considering their mineral-melt partition coefficients (e.g. Hirschmann, 2000). At low pressures, i.e. <2 GPa, the presence of alkalies has a strong effect on lowering the peridotite solidus temperature (Hirschmann, 2000), however, as Na_2O, for example, becomes more compatible in clino-pyroxene with increasing pressure (e.g. D_{Na} $\sim$0.05 at 0.1 GPa; $\sim$0.3 at 4 GPa, (Blundy et al., 1995)), this effect should become less pronounced. At pressures above 20 GPa D_{Na} between ferropericlase and liquid increases with increasing pressure from 0.35 to 0.63 at 24 GPa (Herzberg and Zhang, 1996); Trønnes and Frost, 2002) and is >1 at 33 GPa (Ito et al., 2004). Its effect on the solidus temperature is, therefore, likely trivial at lower mantle conditions. Ni is compatible in ferropericlase and Cr and Ti have partition coefficients close to unity in the pressure range 24–33 GPa (Trønnes and Frost, 2002; Ito et al., 2004). Many trace elements are also highly compatible in CaPv (Corgne and Wood, 2002), thus minor and trace elements are expected to have little effect on the lower mantle solidus. The only exceptions are potentially H_2O and CO_2, however, in the bulk of the lower mantle C is most likely in a reduced form that will not influence melting (Stagno et al., 2011) and H_2O is unlikely to be present in sufficient concentrations to cause significant effects. Generally, minor, trace and volatile elements will have some effect in depressing the solidus temperature but will have little effect once the degree of melting increases above that where the melt is volatile dominated.

Recent diamond anvil experiments performed to pressures of 159 GPa (Nomura et al., 2011) indicate a significant change in Fe–Mg partitioning between Mg-perovskite and silicate liquid at $\sim$76 GPa proposed to result from a spin transition of Fe in the melt. If correct, the main influence on the melting relations would likely be as a result of more FeO partitioning into the liquid at the solidus, thus lowering the solidus temperature. Nomura et al. (2011) could not measure melting temperatures such that absolute effects on the solidus are not known. However, the solidus temperature determinations of Fiquet et al. (2010) or Andrault et al. (2011) certainly show no clear indication for this effect. An estimate for the drop in solidus temperature can be made by considering the Mg-perovskite—liquid K_d above 76 GPa (i.e. $K_d^{MgPv-liq}=0.07$; Nomura et al., 2011). Assuming Fe–Mg partitioning between Mg-perovskite and ferropericlase at $\sim$100 GPa (Auzende et al., 2008) and an SiO_2 content at the eutectic of 40 mol% (Fig. 5), results in a eutectic liquid containing 14 mol% FeO at the CMB. Assuming the depression of melting due to FeO remains the same in both spin states, this would correspond to a depression in the solidus temperature of $\sim$600 K relative to the simple MgO–$MgSiO_3$ eutectic temperature. This would shift the solidus down by $\sim$200 K more than if this proposed Fe spin transition is ignored. Given that FeO likely has the largest effect of any additional major element on the mantle solidus, it is crucial that more data are obtained on the partitioning and melting depression effects of FeO at CMB conditions.

5.2. Implications for ultra-low velocity zones at the base of the mantle

Seismic studies provide evidence for regions within the D″ layer of the mantle just above the CMB where significant localised reductions in both P- and S- wave velocities occur (e.g. Garnero and Helmberger, 1998). These so called ultra-low velocity zones (ULVZ) are typically between 5 and 40 km thick and characterised

by a relatively sharp transition from the overlying mantle. These regions have been proposed to result from the presence of partial melt above the CMB. The possibility that a BSE lower mantle composition is melting at the CMB can be examined by comparing the estimated mantle solidus temperature with estimates for the temperature gradient in the thermal boundary region at the CMB.

The mantle temperature gradient near the CMB will depend on the mantle geotherm and the temperature at the top of the outer core, in addition to the thermal conductivity across this gradient. The temperature of the outer core can be derived from theoretical or experimentally determined (or extrapolated) freezing point temperatures of potential core-liquids at the inner-core boundary (ICB). Knowledge of this "anchor" temperature then allows the temperature at the CMB to be calculated by assuming an adiabatic temperature gradient. However, even the melting temperature of pure Fe at the ICB remains controversial (e.g. Boehler, 2000; Nguyen and Holmes, 2004) and the unknown proportions of light elements in the core (e.g. Birch, 1952; Poirier, 1994), and their effect on melting temperature lead to a range of temperatures at the outermost core, with current best estimates in the range 3500–4400 K (e.g. Boehler, 2000; Alfe et al., 2004; Morard et al., 2011; Murphy et al., 2011). It has been proposed that certain dual seismic reflectors detected at the base of the mantle can be used to estimate two temperatures along the steep thermal gradient at the CMB by assuming an origin related to double crossing of the phase boundary between perovskite and post perovskite (PPv) (Murakami et al., 2004). Such an assessment is currently difficult given the uncertainties in the depth and Clapeyron slope of the MgPv–PPv transition (Tateno et al., 2009) and uncertainty as to the effects of Al and Fe substitution on the depth and sharpness of the phase boundary (Catalli et al., 2009).

The range of estimated CMB temperatures and mantle geotherms are included in Fig. 7. A comparison with the FeO–MgO–$MgSiO_3$ model melting temperatures indicates that the BSE solidus at the CMB could only be crossed if temperatures at the CMB correspond to those at the very top end of the estimated range. This is a similar conclusion as would be drawn from the results of Holland and Ahrens (1997), Andrault et al. (2011) and Fiquet et al. (2010).

A further interesting point, however, is that if ULVZs are caused by melting, the apparent sharp transition in velocity requires that the melt fraction increases rapidly over a short depth interval. Estimates for the absolute values of the melt volume fraction required range between 0.05 and 0.3, depending on melt distribution and geometry (Williams and Garnero, 1996) and may be around 0.15, consistent with an observed ratio in S- to P-wave reduction of 3:1 (Hier-Majumder, 2008). High melt fractions over a narrow depth range can be obtained if the temperature interval between solidus and liquidus is relatively small. This small estimated melting interval is the main prediction from our model that deviates from the previous experimental studies. Based on our model we estimate that temperature increases as small as 15–20 K above the solidus may be sufficient to produce a melt fraction of 0.15. This means that if temperatures are close to those of the BSE solidus at the CMB then very small lateral thermal fluctuations could lead to the formation of ULVZs.

Recent studies suggest a spatial correlation between ULVZs and other larger seismic anomalies, the Large Low Shear Wave Velocity Provinces (LLSVP), which spread across significant parts of the base of the lower mantle beneath Africa and the Pacific (McNamara et al., 2010). The origin of LLSVPs, their composition and thermal structure is debated (e.g. see review of Lay and Garnero (2011)) but the low shear wave velocity compared to average mantle indicates the presence of either relatively hot or dense material, or both. The most likely explanation for elevated density would be enrichment of FeO, which, as argued above, is likely to be the most effective major component in depressing the silicate solidus and liquidus. Our results imply that small increases in local FeO content would have a similar effect to small increases in temperature i.e. can result in large melt fractions developing over small depth intervals. Thus a combination of higher temperatures and FeO enrichment compared to average mantle would indeed support a correlation of LLSVPs and ULVZs and favour partial melting as the origin of the latter. If this is the case then it is not likely to be BSE composition mantle that is melting to form ULVZs. ULVZs have also been detected outside LLSVP regions (McNamara et al., 2010) for which a plausible explanation may be small scale interaction and oxidation of outer core material causing raised mantle FeO contents, which could either lead to melting or to a reduction in seismic wave velocity due to Fe-enrichment of ferropericlase as observed by Wicks et al. (2010). Other alternative explanations for the origin of ULVZs include sharp compositional gradients in mantle rocks, which could be remnants from magma ocean crystallisation, particularly if such magmas become negatively buoyant towards the CMB (Labrosse et al., 2007).

6. Conclusions

Melting phase relations in the system MgO–$MgSiO_3$ were precisely determined using multianvil devices between 16 and 26 GPa. A multichamber sample approach ensures internally consistent results and precise determination of eutectic composition, which places hard constraints on the thermodynamics of silicate melting. We parameterise the present data using equations of state from the literature to calculate properties for end-member solid and liquid phases of MgO and $MgSiO_3$ and a simple thermodynamic model for mixing of the liquid.

Extrapolating the thermodynamic model to pressures at the core mantle boundary (CMB) shows that the eutectic composition eventually becomes near constant at a mole fraction of SiO_2 of $\sim$0.4. We show that melting relations of natural peridotite at lower mantle conditions can be well described on the basis of phase relations of the simple binary, especially when the effects of FeO on melting temperatures are estimated. The thermodynamic model predicts that the solidus and liquidus for a peridotite composition are never more than $\sim$250 K apart and that the solidus temperature at the CMB is approximately 4400 ± 300 K. Our data, therefore, indicate that partial melting at the base of the mantle is possible in a peridotite composition only if temperatures are at the high end of the currently best estimated range of 3600–4400 K at the CMB. Then partial melting could indeed be a likely explanation for the origin of seismic ultra-low velocity zones at the CMB. The small temperature interval between solidus and liquidus allows large melt fractions to form through relatively small temperature fluctuations, providing a good explanation for the sharpness of the seismic velocity profiles. Alternatively, local variations in chemistry across the CMB due to interaction with the core and enrichment in FeO could also be responsible for the localised occurrence of the ultra-low velocity zones.

Acknowledgements

We would like to thank H. Fischer, H. Schultz and D. Krauße for their technical assistance. N. de Koker and Mark Caddick provided fruitful discussions. C.L. thanks Jamie Connolly for support with Perple_X. Reviews by Reidar Trønnes and Paul Asimow provided valuable improvement to the manuscript.

Appendix A. Supporting information

Supplementary data associated with this article can be found in the online version at http://dx.doi.org/10.1016/j.epsl.2012.06.038.

References

Alfe, D., 2005. Melting curve of MgO from first-principles simulations. Phys. Rev. Lett., 94.

Alfe, D., Price, G.D., Gillan, M.J., 2004. The melting curve of iron from quantum mechanics calculations. J. Phys. Chem. Solids 65, 1573–1580.

Andrault, D., Bolfan-Casanova, N., Nigro, G.L., Bouhifd, M.A., Garbarino, G., Mezouar, M., 2011. Solidus and liquidus profiles of chondritic mantle: implication for melting of the Earth across its history. Earth Planet. Sci. Lett. 304, 251–259.

Auzende, A.-L., Badro, J., Ryerson, F.J., Weber, P.K., Fallon, S.J., Addad, A., Siebert, J., Fiquet, G., 2008. Element partitioning between magnesium silicate perovskite and ferropericlase: new insights into bulk lower-mantle geochemistry. Earth Planet. Sci. Lett. 269, 164–174.

Belonoshko, A.B., Dubrovinsky, L.S., 1996. Molecular dynamics of NaCl (B1 and B2) and MgO (B1) melting: two-phase simulation. Am. Mineral. 81, 303–316.

Birch, F., 1952. Elasticity and constituents of the Earth interior. J. Geophys. Res. 57, 227–286.

Blundy, J.D., Falloon, T.J., Wood, B.J., Dalton, J.A., 1995. Sodium partitioning between clinopyroxene and silicate melts. J. Geophys. Res. 100, 15501–15515.

Boehler, R., 2000. High-pressure experiments and the phase diagram of lower mantle and core materials. Rev. Geophys. 38, 221–245.

Bowen, N.L., Anderson, O., 1914. The binary system MgO–SiO_2. Am. J. Sci. 37, 487–5000.

Boyd, F.R., England, J.L., Davis, B.T.C., 1964. Effects of pressure on the melting and polymorphism of enstatite, $MgSiO_3$. J. Geophys. Res. 69, 2101–2109.

Boyet, M., Carlson, R.W., 2005. Nd-142 evidence for early (>4.53 Ga) global differentiation of the silicate Earth. Science 309, 576–581.

Canup, R.M., Asphaug, E., 2001. Origin of the Moon in a giant impact near the end of the Earth's formation. Nature 412, 708–712.

Catalli, K., Shim, S.-H., Prakapenka, V., 2009. Thickness and Clapeyron slope of the post-perovskite boundary. Nature 462, 782–785.

Chen, C.H., Presnall, D.C., 1975. The system Mg_2SiO_4–SiO_2 at pressures up to 25 kilobars. Am. Mineral. 60, 398–406.

Cohen, R.E., Gong, Z., 1994. Melting and melt structure of MgO at high pressures. Phys. Rev. B 50, 12301–12311.

Connolly, J.A.D., 1990. Multivariable phase diagrams—an algorithm based on generalized thermodynamics. Am. J. Sci. 290, 666–718.

Corgne, A., Wood, B.J., 2002. $CaSiO_3$ and $CaTiO_3$ perovskite-melt partitioning of trace elements: implications for gross mantle differentiation. Geophys. Res. Lett. 29 (19)http://dx.doi.org/10.1029/2001gl014398.

Davis, B.T.C., England, J.L., 1964. The melting of forsterite up to 50 kilobars. J. Geophys. Res. 69, 1113–1116.

de Koker, N., 2008. Liquid State Physics of the MgO–SiO_2 System at Deep Mantle Pressures. Ph.D. Thesis. University of Michigan, pp. 143.

de Koker, N., Stixrude, L., 2009. Self-consistent thermodynamic description of silicate liquids, with application to shock melting of MgO periclase and $MgSiO_3$ perovskite. Geophys. J. Int. 178, 162–179.

Finger, L.W., Hazen, R.M., Prewitt, C.T., 1991. Crystal structures of $Mg_{12}Si_4O_{19}(OH)_2$ (phase B) and $Mg_{14}Si_5O_{24}$ (phase AnhB). Am. Mineral. 76, 1–7.

Fiquet, G., Auzende, A.L., Siebert, J., Corgne, A., Bureau, H., Ozawa, H., Garbarino, G., 2010. Melting of peridotite to 140 gigapascals. Science 329, 1516–1518.

Frost, D.J., Liebske, C., Langenhorst, F., McCammon, C.A., Tronnes, R.G., Rubie, D.C., 2004a. Experimental evidence for the existence of iron-rich metal in the Earth's lower mantle. Nature 428, 409–412.

Frost, D.J., Poe, B.T., Tronnes, R.G., Liebske, C., Duba, A., Rubie, D.C., 2004b. A new large-volume multianvil system. Phys. Earth Planet. Inter. 143–144, 507–514.

Garnero, E.J., Helmberger, D.V., 1998. Further structural constraints and uncertainties of a thin laterally varying ultralow-velocity layer at the base of the mantle. J. Geophys. Res. 103, 12495–12509.

Gasparik, T., 1990. Phase relations in the transition zone. J. Geophys. Res. 95 (B10), 15751–15769.

Herzberg, C., Zhang, J.Z., 1996. Melting experiments on anhydrous peridotite KLB-1: compositions of magmas in the upper mantle and transition zone. J. Geophys. Res. 101, 8271–8295.

Hier-Majumder, S., 2008. Influence of contiguity on seismic velocities of partially molten aggregates. J. Geophys. Res., 113, http://dx.doi.org/10.1029/2008jb005662.

Hirschmann, M.M., 2000. Mantle solidus: experimental constraints and the effects of peridotite composition. Geochem. Geophys. Geosyst. 1, 26, http://dx.doi.org/10.1029/2000GC000070.

Holland, K.G., Ahrens, T.J., 1997. Melting of $(Mg,Fe)_2SiO_4$ at the core–mantle boundary of the Earth. Science 275, 1623–1625.

Ito, E., Katsura, T., 1992. Melting of ferromagnesian silicates under the lower mantle conditions. In: Syono, Y., Manghnani, M.H. (Eds.), High-Pressure Research: Application to Earth and Planetary Sciences. American Geophysical Union, pp. 315–322.

Ito, E., Kubo, A., Katsura, T., Walter, M.J., 2004. Melting experiments of mantle materials under lower mantle conditions with implications for magma ocean differentiation. Phys. Earth Planet. Inter. 143–144, 397–406.

Katsura, T., Yamada, H., Nishikawa, O., Song, M.S., Kubo, A., Shinmei, T., Yokoshi, S., Aizawa, Y., Yoshino, T., Walter, M.J., Ito, E., Funakoshi, K., 2004. Olivinewadsleyite transition in the system $(Mg,Fe)2SiO_4$. J. Geophys. Res. 109, http://dx.doi.org/10.1029/2003jb002438.

Kato, T., Kumazawa, M., 1985a. Effect of high pressure on the melting relation in the system Mg_2SiO_4–$MgSiO_3$, I, eutectic relation up to 7 GPa. J. Phys. Earth 33 514-254.

Kato, T., Kumazawa, M., 1985b. Stability of phase B, a hydrous magnesium silicate to 2300 °C at 20 GPa. Geophys. Res. Lett. 12, 534–535.

Kato, T., Kumazawa, M., 1986. Melting and phase relation in the system Mg_2SiO_4–$MgSiO_3$ at 20 GPa under hydrous conditions. J. Geophys. Res. 91 (B9), 9351–9355.

Kato, T., Kumazawa, M., 1990. High pressure effect on melting relations in the system Mg_2SiO_4–$MgSiO_3$: phase transitions in the constituent phases and differentiation by melting in the Earth's mantle. In: Marumo, F. (Ed.), Dynamic Processes of Material Transport and Transformation in the Earth's Interior. Terra Scientific Publishing Company, Tokyo, pp. 277–308.

Kato, T., Nakata, N., Ohtani, E., Onuma, K., 1998. Melting experiments on the forsterite–pyrope system at 8 and 13.5 GPa. Phys. Earth Planet. Inter. 107, 97–102.

Keppler, H., Frost, D.J., 2005. Introduction to minerals under extreme conditions. In: Miletich, R. (Ed.), Mineral Behavior at Extreme Conditions. European Mineralogical Union, pp. 1–30.

Kudo, R., Ito, E., 1996. Melting relations in the system $Mg_4Si_4O_{12}$(En)–$Mg_3Al_2Si_3O_{12}$(Py) at high pressures. Phys. Earth Planet. Inter. 96, 159–169.

Labrosse, S., Hernlund, J.W., Coltice, N., 2007. A crystallizing dense magma ocean at the base of the Earth's mantle. Nature 450, 866–869.

Lay, T., Garnero, E.J., 2011. Deep mantle seismic modeling and imaging. Annu. Rev. Earth Planet. Sci. 39, 91–123.

Lay, T., Garnero, E.J., Williams, Q., 2004. Partial melting in a thermo-chemical boundary layer at the base of the mantle. Phys. Earth Planet. Inter. 146, 441–467.

Liebske, C., Corgne, A., Frost, D.J., Rubie, D.C., Wood, B.J., 2005. Compositional effects on element partitioning between Mg-silicate perovskite and silicate melts. Contrib. Mineral. Petrol. 149, 113–128.

Liu, T.C., Presnall, D.C., 1990. Liquidus phase relationships on the join anorthite–forsterite–quartz at 20 kbar with application to basalt petrogenesis and igneous spphirine. Contrib. Mineral. Petrol. 104, 735–742.

Matas, J., Bass, J., Ricard, Y., Mattern, E., Bukowinski, M.S.I, 2007. On the bulk composition of the lower mantle: predictions and limitations from generalized inversion of radial seismic profiles. Geophys. J. Int. 170, 764–780, http://dx.doi.org/10.1111/j.1365-246X.2007.03454.x.

McKenzie, D., Bickle, M.J., 1988. The volume and compositionof melt generated by extension of the lithosphere. J. Petrol. 29, 625–679.

McMillan, P.F., Hemley, R.J., Gillet, P., 1996. Vibrational spectroscopy of mantle minerals. In: Dyar, M.D., McCammon, C.A., Schaefer, M.W. (Eds.), Mineral Spectroscopy: A Tribute to Roger G. Burns. The Goechemical Society.

McNamara, A.K., Garnero, E.J., Rost, S., 2010. Tracking deep mantle reservoirs with ultra-low velocity zones. Earth Planet. Sci. Lett. 299, 1–9.

Mitchell, R.H., 1986. Kimberlites. Mineralogy, Geochemistry, and Petrology. Plenum Press, New York, London.

Morard, G., Andrault, D., Guignot, N., Siebert, J., Garbarino, G., Antonangeli, D., 2011. Melting of Fe–Ni–Si and Fe–Ni–S alloys at megabar pressures: implications for the core-mantle boundary temperature. Phys. Chem. Miner. 38, 767–776.

Mosenfelder, J.L., Asimow, P.D., Frost, D.J., Rubie, D.C., Ahrens, T.J., 2009. The $MgSiO_3$ system at high pressure: thermodynamic properties of perovskite, postperovskite, and melt from global inversion of shock and static compression data. J. Geophys. Res., 114, http://dx.doi.org/10.1029/2008jb005900.

Murakami, M., Hirose, K., Kawamura, K., Sata, N., Ohishi, Y., 2004. Post-perovskite phase transition in $MgSiO_3$. Science 304, 855–858.

Murphy, C.A., Jackson, J.M., Sturhahn, W., Chen, B., 2011. Melting and thermal pressure of hcp-Fe from the phonon density of states. Phys. Earth Planet. Inter. 188, 114–120.

Nguyen, J.H., Holmes, N.C., 2004. Melting of iron at the physical conditions of the Earth's core. Nature 427, 339–342.

Nishihara, Y., Matsukage, K.N., Karato, S.I., 2006. Effects of metal protection coils on thermocouple EMF in multi-anvil high-pressure experiments. Am. Mineral. 91, 111–114.

Nomura, R., Ozawa, H., Tateno, S., Hirose, K., Hernlund, J., Muto, S., Ishii, H., Hiraoka, N., 2011. Spin crossover and iron-rich silicate melt in the Earth's deep mantle. Nature 473, 199–202.

Ohtani, E., Kumazawa, M., 1981. Melting of forsterite Mg_2SiO_4 up to 15 GPa. Phys. Earth Planet. Inter. 27, 32–38.

Ohtani, E., Moriwaki, K., Kato, T., Onuma, K., 1998. Melting and crystal-liquid partitioning in the system Mg_2SiO_4–Fe_2SiO_4 to 25 GPa. Phys. Earth Planet. Inter., 75–82.

Poirier, J.-P., 1994. Light elements in the Earth's outer core: a critical review. Phys. Earth Planet. Inter. 85, 319–337.

Presnall, D.C., Gasparik, T., 1990. Melting of enstatite ($MgSiO_3$) from 10 to 16.5 GPa and the forsterite (Mg_2SiO_4)–majorite ($MgSiO_3$) eutectic at 16.5 GPa: implications for the origin of the mantle. J. Geophys. Res. 95 (B10), 15771–15777.

Presnall, D.C., Walter, M.J., 1993. Melting of forsterite, Mg_2SiO_4, from 9.7 to 16.5 GPa. J. Geophys. Res. 98 (B11), 19777–19783.
Presnall, D.C., Weng, Y.H., Milholland, C.S., Walter, M.J., 1998. Liquidus phase relations in the system MgO–$MgSiO_3$ at pressures up to 25 GPa—constraints on crystallization of molten Hadean mantle. Phys. Earth Planet. Inter. 107, 83–95.
Shen, G.Y., Lazor, P., 1995. Measurement of melting temperatures of some minerals under lower mantle pressures. J. Geophys. Res. 100, 17699–17713.
Sinmyo, R., Hirose, K., 2010. The Soret diffusion in laser-heated diamond-anvil cell. Phys. Earth Planet. Inter. 180, 172–178.
Stagno, V., Tange, Y., Miyajima, N., McCammon, C.A., Irifune, T., Frost, D.J., 2011. The stability of magnesite in the transition zone and the lower mantle as function of oxygen fugacity. Geophys. Res. Lett. 38 http://dx.doi.org/10.1016/j.epsl.2010.09.038.
Stevenson, D.J., 1990. Fluid dynamics of core formation. In: Newsom, H.E., Jones, J.H. (Eds.), Origin of the Earth. Oxford Univ., New York, pp. 231–249.
Stixrude, L., Lithgow-Bertelloni, C., 2011. Thermodynamics of mantle minerals—II. Phase equilibria. Geophys. J. Int. 184, 1180–1213.
Taylor, H.C.J, 1973. Melting relations in the system MgO-Al_2O_3-SiO_2 at 15 kb. Geol. Soc. Am. Mem. 84, 1335–1348.
Tateno, S., Hirose, K., Sata, N., Ohishi, Y., 2009. Determination of post-perovskite phase transition boundary up to 4400 K and implications for thermal structure in D″ layer. Earth Planet. Sci. Lett. 277, 130–136.
Tonks, W.B., Melosh, H.J., 1993. Magma ocean formation due to giant impacts. J. Geophys. Res. 98 (E3), 5319–5333.
Trønnes, R.G., Frost, D.J., 2002. Peridotite melting and mineral-melt partitioning of major and minor elements at 22–24.5 GPa. Earth Planet. Sci. Lett. 197, 117–131.
Wicks, J.K., Jackson, J.M., Sturhahn, W., 2010. Very low sound velocities in iron-rich (Mg,Fe)O: implications for the core–mantle boundary region. Geophys. Res. Lett., 37, http://dx.doi.org/10.1029/2010gl043689.
Williams, Q., Garnero, E.J., 1996. Seismic evidence for partial melt at the base of Earth's mantle. Science 273, 1528–1530.
Wood, B.J., 2000. Phase transformations and partitioning relations in peridotite under lower mantle conditions. Earth Planet. Sci. Lett. 174, 341–354.
Zerr, A., Boehler, R., 1993. Melting of (Mg,Fe)SiO3-perovskite to 625 kilobars—indication of a high-melting temperature in the lower mantle. Science 262, 553–555.
Zerr, A., Boehler, R., 1994. Constraints on the melting temperature of the lower mantle from high-pressure experiments on MgO and magnesiowustite. Nature 371, 506–508.
Zerr, A., Serghiou, G., Boehler, R., 1997. Melting of $CaSiO_3$ perovskite to 430 kbar and first in-situ measurements of lower mantle eutectic temperatures. Geophys. Res. Lett. 24, 909–912.
Zhang, J., Herzberg, C., 1994. Melting experiments on anhydrous peridotite KLB-1 from 5.0 to 22.5 GPa. J. Geophys. Res. 99 (B9), 17729–17742.
Zhang, L., Fei, Y., 2008. Melting behavior of (Mg,Fe)O solid solutions at high pressure. Geophys. Res. Lett. 35 http://dx.doi.org/10.1029/2008gl034585.